Article

Sustainable microalgae extraction for proactive water bloom prevention

Mengran Wu[1,5], Chen Zhang ®[2,5], Xiqing Xie[1], Huajun Feng[1,3], Ghim Wei Ho ®[2,4] ✉ & Yingfeng Xu ®[1,2,3] ✉

The recurring and unpredictable occurrences of water blooms have emerged as an escalating global threat to both the environment and water resources. Superior to the unsatisfactory post-bloom treatment techniques, the proactive strategy of reducing microalgae density in an economical and safe manner holds promise for effective water bloom control and prevention; however, it remains an important challenge. Here we report an efficient microalgae extraction mediated by a sustainable microalgae grabber (SMAG), which fully integrates tailored water depth suspending, electrostatic microalgae capture and magnetic collection. More importantly, the photothermal conversion capability of SMAG allows for the denaturation of extracellular polymeric substances, enabling on-demand desorption of microalgae for desired multiple reuses. Through the cyclic operation of these recyclable SMAGs, it demonstrates a remarkable microalgae removal efficiency of 94% and photothermal-driven spontaneous desorption, with a recovery efficiency of over 90%. Furthermore, a customized self-cruising floating device has been designed for the large-scale implementation of SMAGs, showcasing solar-powered sustainable microalgae extraction and harvesting in natural water bodies. The customizable and scalable SMAG offers a refreshing perspective in reinvigorating industries related to proactive water bloom prevention and microalgae resource capitalization.

The escalating frequency and severity of water blooms worldwide, characterized by the rapid and excessive proliferation of microalgae, have emerged as an increasingly dire threat to aquatic environments, public health, water resources and the global economy[1–3]. Water blooms result from a complex interplay of environmental factors, including nutrient excess[4], temperature[5], light and water-flow dynamics[6], making their occurrence highly variable in temporal and spatial scales[7]. These elusive variables pose substantial challenges in the early prediction and post-remediation of water blooms[8–10]. On the contrary, a proactive approach to sustainably reduce microalgae concentrations through selective extraction and harvesting, in an economical and environmentally safe manner, shows potential for effective water bloom prevention[11,12]. Additionally, the deep processing of the collected microalgae byproduct can further produce valuable biomass, offering potential solutions to alleviate the current energy crisis[13–16]. Therefore, the development of a specialized technique for sustainable microalgae extraction is crucial from the perspectives of both environmental governance and resource exploitation.

[1]School of Environmental Science and Engineering, Zhejiang Gongshang University, Hangzhou, China. [2]Department of Electrical and Computer Engineering, National University of Singapore, Singapore, Singapore. [3]International Science and Technology Cooperation Platform for Low-Carbon Recycling of Waste and Green Development, Zhejiang Gongshang University, Hangzhou, China. [4]Department of Materials Science and Engineering, National University of Singapore, Singapore, Singapore. [5]These authors contributed equally: Mengran Wu, Chen Zhang. ✉e-mail: elehgw@nus.edu.sg; yingfengxu@zjgsu.edu.cn
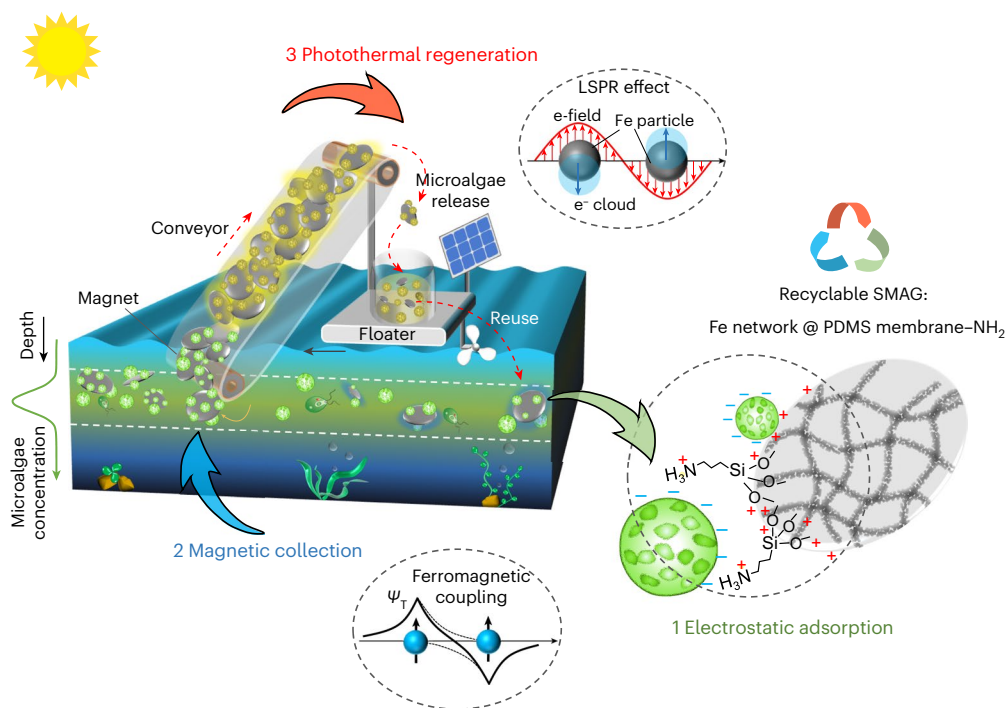
Fig. 1 | Design principle of recyclable SMAGs for sustainable microalgae extraction. A schematic diagram demonstrating efficient electrostatic microalgae adsorption (1), magnetic collection of the microalgae-saturated SMAGs (2) and photothermal-driven desorption/regeneration process (3). These three successive steps can be integrated into a solar cell-powered self-cruising floating device; thus, SMAGs could realize sustainable microalgae extraction for proactive water bloom prevention in large water bodies. LSPR denotes localized surface plasmon resonance.

Despite efficient off-site microalgae harvesting using various traditional techniques[17,18], such as centrifugation[19], filtration[20,21], flotation and flocculation[22–24], they are generally inappropriate or inadequate for proactive water bloom prevention[10,12]. This necessitates the development of an on-site selective microalgae extraction method in natural water bodies. Unencumbered by costly professional equipment and safety concerns related to chemical additives[17,25,26], the functional adsorbers employing efficient physicochemical affinity towards microalgae offer promising solutions. Nevertheless, the design of adsorbers presents critical challenges due to numerous practical considerations. First, in contrast to most aquatic organisms, microalgae predominantly thrive at a specific depth beneath the water surface, where light for photosynthesis is optimal but not excessive[1–3]. Such a spatial discrepancy in species density enhances the selectivity of microalgae extraction, but also underlines a critical functionality of adsorbers, namely the ability to target and remain suspended at the desired water depth for optimal capture. Second, the ideal adsorbers should overcome the disposability or 'single-use' limitation of conventional ones. Their gentle regeneration, devoid of energy-intensive mechanical or harsh chemical treatments, is essential for the sustainability of continuous microalgae extraction[27]. Finally, to pre-emptively mitigate the intracellular production of microcystin and eliminate its potential release, it is desirable to deactivate the extracted microalgae while preserving the integrity of the cell membrane[28].

In this Article, drawing on the physiological characteristics of microalgae, we demonstrate the solar-powered microalgae extraction for proactive water bloom, achieved through the development of a sustainable microalgae grabber (SMAG). The SMAGs feature all-encompassing built-in functionalities of depth-tailored suspension, electrostatic microalgae adsorption coupled with the magnetic collection, and photothermal regeneration accompanied by synchronous microalgae deactivation. As shown in Fig. 1, SMAGs of customizable density are designed to freely remain suspended in the microalgae aggregation layer at the desired water depth, harmonizing with natural flow fluctuations. Subsequently, they can electrostatically capture microalgae with a certain degree of selectivity from the targeted aquatic system (Supplementary Table 1). Following magnetic collection, separation and subsequent solar-driven photothermal treatment, the microalgae-saturated SMAGs enable on-demand desorption accompanied by efficient deactivation of microalgae, thus facilitating the regeneration of the SMAG for multiple reuses. More importantly, further integration with a self-cruising floating device allows SMAGs to undertake unsupervised water bloom prevention in large water bodies.

Results

Design and construction of SMAGs

With environmental safety and low cost in mind, the conceived SMAG is engineered as a composite membrane composed of an amino-modified polydimethylsiloxane (PDMS) matrix encapsulating a zero-valent iron particle network inside (Fig. 1 and Supplementary Note 1). The former imparts a positively charged surface to the SMAGs, enabling the electrostatic adsorption of microalgae that consistently exhibit a negatively charged surface in general aquatic environments[29]. The latter iron nanoparticles (FeNPs; Supplementary Fig. 1), serving as the ferromagnetic and photothermal component, were prepared using a modified Hubble-bubble method[30,31]. These particles are amorphous and tens of nanometres in diameter (Fig. 2a and Supplementary Figs. 1d and 2), as confirmed by a transmission electron microscope (TEM), selected-area electron diffraction and X-ray diffraction. The identified 2.6-nm-thick shell (Supplementary Fig. 2a) shields the metastable zero-valent iron inner core from oxidation (Supplementary Fig. 3). Owing to the absence of well-defined crystalline structure (Supplementary Fig. 2b), the amorphous FeNPs lack magnetocrystalline anisotropy[32]. Compared with their crystalline counterparts, this unique property of low coercivity endows them with considerably superior dispersibility in solution and more responsive behaviour to external magnetic fields[30], beneficial for on-demand magnetic collection (Supplementary Fig. 1a–c).
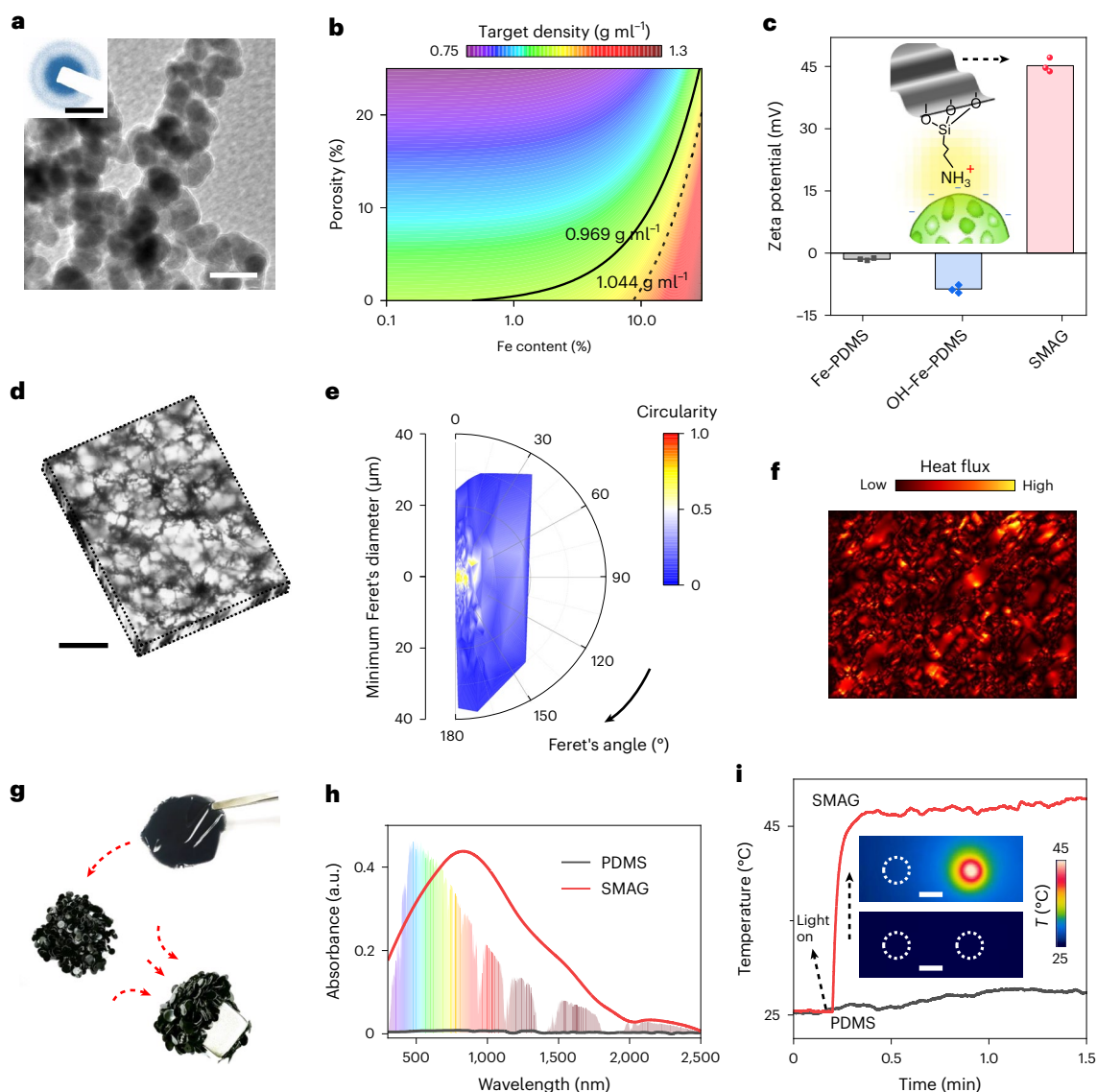
**Fig. 2 | Construction and characterizations of the functional SMAGs.**
a, TEM image of the FeNPs. Scale bar, 50 nm. The inset shows the corresponding selected area electron diffraction pattern. Scale bar, 10 nm⁻¹. **b**, Customized Fe content and porosity of the SMAGs to meet the target density for the water body. The colour represents the density of the SMAGs as indicated by the colour bar on the top. The black solid and dotted lines represent the lowest and highest densities of natural water bodies, respectively. **c**, Zeta potential of the Fe–PDMS, OH–Fe–PDMS and SMAG. The bars represent mean values, $n = 3$ for each group. The inset illustrates the electrostatic interaction between the SMAG and microalgae. **d**, Three-directional tomographic reconstitution of the SMAG.

Scale bar, 50 µm. **e**, Geometrical analysis of the FeNPs network in the SMAG, including the Feret properties and circularity estimation. **f**, A simulation of in-plane heat flow diffusion in the SMAG. **g**, Digital photos showing the customizable and mass-producible preparation of the SMAGs, which can be instantly collected by applying a magnetic field. **h**, The absorption spectra of the SMAGs and pure PDMS, and spectral solar irradiance (AM 1.5). a.u., arbitrary units. **i**, Time-course temperature curves of the SMAG and PDMS under irradiation. The insets show the corresponding thermal images of the PDMS (left) and SMAG (right) recorded at 0 s (bottom) and 20 s (top) under simulated solar illumination. Scale bars, 1 mm.

Subsequently, using an interfacial tape casting approach, the as-produced FeNPs were encapsulated into PDMS to form a flexible membrane (Fe–PDMS). According to the density of the target water body that is determined by the salinity and temperature, the membrane density can be accurately adjusted by changing the FeNPs content and porosity (Fig. 2b). This allows the SMAGs to target and remain suspended at the desired depth in any water body (Supplementary Fig. 4), we selected natural freshwater with a density of 1.01 g cm⁻³ for this study. Through plasma oxygen treatment (denoted as OH–Fe–PDMS) and cross-linking with amino siloxane, the surface amino-group functionalization was successfully achieved (Supplementary Fig. 5) without influencing the structure of PDMS matrix (Supplementary Fig. 6). The amino groups act as proton acceptors to adsorb H⁺ ions from the

surrounding solution; thus, the modification improves hydrophilicity (Supplementary Fig. 7) and induces a positively charged surface even in neutral aqueous solution (Fig. 2c).

The encapsulated FeNPs were found to spontaneously assemble into a disordered and isotropous network, as revealed by three-dimensional tomographic reconstitution (Fig. 2d,e). Benefitting from the engineered continuous FeNPs network and the intrinsic low thermal conductivity of the PDMS matrix, the heat flux is intense and highly localized within the membrane, leading to minimal heat dissipation at the boundaries, as verified by the geometric heat diffusion simulation (Fig. 2f). This indicates a rapid spatial homogenization of the photothermally generated heat throughout the entire matrix. A simple laser cutting procedure enables large-scale production of SMAGs
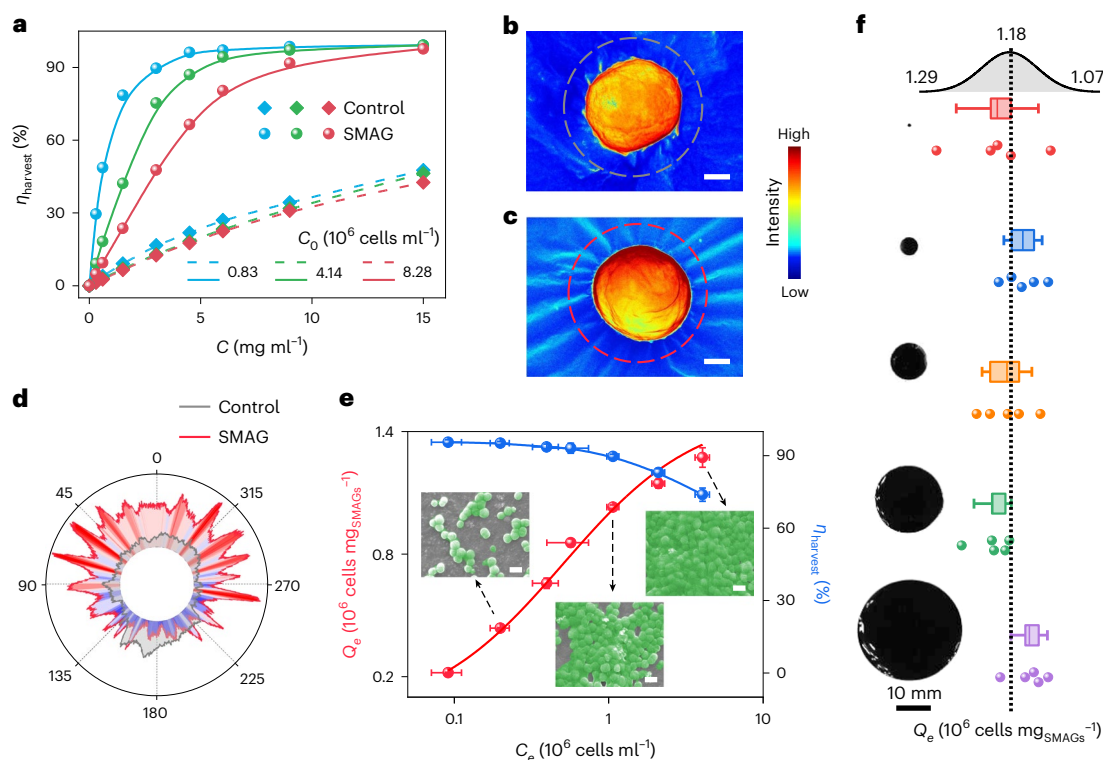
Fig. 3 | Investigation of the adsorption behaviour of microalgae on the SMAGs. a, The dose of SMAGs or Fe–PDMS (control) and *M. aeruginosa* concentration-dependent harvesting efficiency ($\eta_{harvest}$). **b,c**, Pseudo-colour images for an adsorbed *M. aeruginosa* microalga on the Fe–PDMS surface (**b**) and the SMAG surface (**c**). The colour represents the secondary electron scattering intensity as indicated by the colour bar on the right. Scale bars, 1 μm. **d**, Line profiles of secondary electron intensity along the circular lines in **b** and **c**. The intensity values are normalized to that of the plane background. **e**, Adsorption isotherm of microalgae using the SMAGs and the corresponding harvesting efficiency ($\eta_{harvest}$). Scatter data are presented as mean values ± s.d., *n* = 3 for

each group. The adsorption isotherm was fitted with the Langmuir model with an R^2 value of 0.99. The insets are the pseudo-colour SEM images of microalgae adsorbed on the SMAG surface. Scale bars, 5 μm. **f**, Size-independent adsorption capacity (Q_e) of microalgae by SMAGs with varied diameters (range from 0.1 cm to 3 cm). Left: digital photographs of the SMAGs with different diameters. Right: Q_e of microalgae adsorbed by the SMAGs with the corresponding size, *n* = 5 for each group. The box plots represent mean values (centre line), interquartile range (central box) and s.d. (whiskers extending from the box). The distribution of all Q_e values is presented on the top Gaussian fitting curve (black line).

with any customized shapes and dimensions (Supplementary Fig. 8). For the quantitative convenience of the following study, we adopted uniform membranes of 1 mm in diameter and 73 μm in thickness as the SMAGs (Supplementary Figs. 8 and 9a), which exhibit good mechanical durability (Supplementary Figs. 9b and 10) and remarkable sensitivity to the external magnetic field (Fig. 2g and Supplementary Fig. 11). Benefitting from the localized surface plasmon resonance (LSPR) of the encapsulated FeNPs (Supplementary Fig. 12), the SMAGs present a broad spectral absorption that nearly covers the full ultraviolet, visible and near-infrared range of the solar irradiation spectrum[33] (Fig. 2h). As expected, a single discal SMAG exhibited a drastic temperature rise from 25 °C to 45 °C within 10 s of solar illumination (AM 1.5 G and 100 mW cm⁻²; Fig. 2i).

Investigation of the adsorption behaviour

We selected *Microcystis aeruginosa*, one of the most widespread freshwater microalgae that causes harmful algal blooms[34], to investigate the adsorption behaviour of the constructed SMAGs. Through spectral quantification (Fig. 3 and Supplementary Fig. 13), the SMAGs demonstrated excellent microalgae adsorption capabilities, regardless of the initial microalgae concentration. After the development of suspended SMAGs and applying a simulated low-frequency mechanical perturbation for 15 min, the harvesting efficiencies exceed 90% for various initial algae concentrations (Fig. 3a). Compared with the counterpart without amino-group modification (Fe–PDMS), which solely relies on the weak Van der Waals attraction for microalgae adsorption, the additional

incorporation of electrostatic attraction significantly enhances the microalgae adsorption efficiency by 2.5 times.

We further developed an indirect technique to discern the differences in the interaction between the adsorber surface and microalgae. This method relies on the reconstruction of secondary electron scattering intensity to visualize the local strain on the adsorber surface resulting from the microalgae adsorption. Compared with Fe–PDMS (Fig. 3b), the strong tangential force induced by the vertical interaction between the SMAG surface and microalgae resulted in notable surface strain on the elastic surface. The strain is evident from the obvious wrinkles observed around the location where *M. aeruginosa* is adsorbed (Fig. 3c). Further geometric analysis of these wrinkle folds confirms their quasi-periodic angular distribution, suggesting a nearly isotropous electrostatic density on the SMAG surface (Fig. 3d). This characteristic of a quasi-isopotential plane contributes to maximizing the availability of amino groups for microalgae attraction. It is worth mentioning that SMAG's deformable surface enables its spontaneous adjustment to closely conform to the flexible microalgae surface. This leads to a reduction in the distance between attracting pairs, consequently enhancing the electrostatic attraction. The adsorption isotherm fits well with the Langmuir model (Fig. 3e), indicating efficient single-layer adsorption of microalgae on the SMAGs surface with a high K_L value. These theoretical speculations are visually confirmed by the scanning electron microscopy (SEM) observation (insets in Fig. 3e). After a single operation of excess SMAGs in a low-concentration *M. aeruginosa* suspension, their surface is partially covered by scattered microalgae,
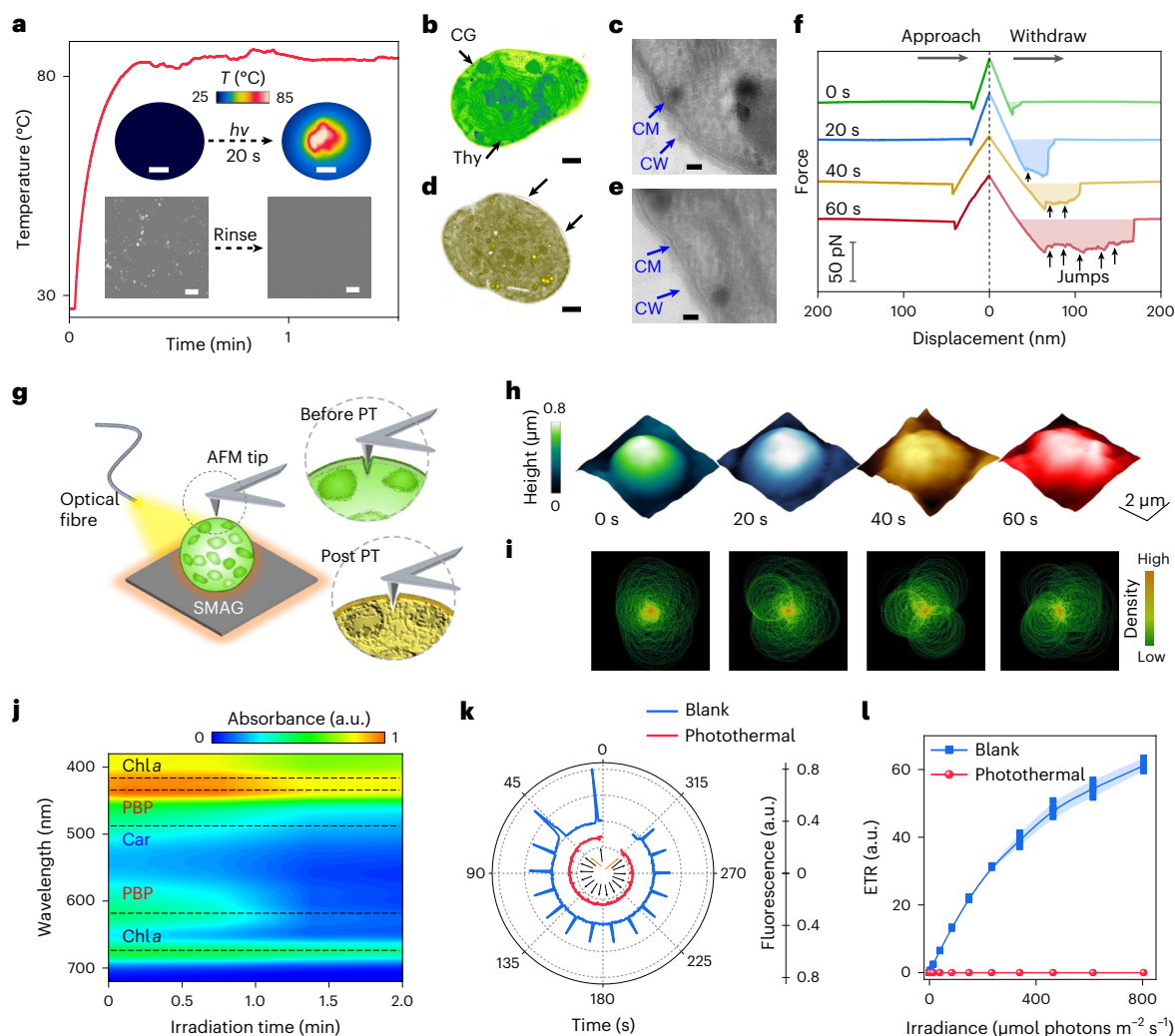
Fig. 4 | Mechanism of photothermal-enabled desorption and deactivation of microalgae. a, Time-course temperature curves of the accumulated microalgae-adsorbed SMAGs under simulated solar irradiation. The top insets are thermal images recorded at 0 s (left) and 20 s (right) under irradiation. Scale bars, 2 cm. The bottom insets are SEM images of the microalgae-adsorbed SMAGs after 2 min photothermal treatment (left) and subsequent DI water rinsing (right). Scale bars, 20 μm. **b,c**, Pseudo-colour TEM images of an initial microalga (**b**) and the corresponding zoomed-in microalga membrane (**c**). **d,e**, Pseudo-colour TEM images of a desorbed microalga from the SMAGs under 2 min illumination (**d**) and the corresponding zoomed-in microalga membrane (**e**). Thy, thylakoids; CG, cyanophycin granules; CW, cell wall; CM, cell membrane. The arrows in **d** indicate the separation between cell wall and membrane. Scale bars, 500 nm (**b** and **d**) and 50 nm (**c** and **e**). **f,g**, AFM force–distance curves (**f**) for the SMAG-adsorbed microalga membrane at different timepoints during irradiation,

and the corresponding illustration of the AFM force measurements during the photothermal treatment (PT) (**g**). **h,i**, AFM topography images (**h**) monitoring the change in a representative SMAG-adsorbed microalga during photothermal treatment (0, 20, 40 and 60 s), along with the corresponding geometrical angular distribution analysis (**i**). The colour bar in **i** indicates the relative density. **j**, Time-resolved absorption spectra of the SMAG-adsorbed microalgae during photothermal treatment. Chl *a*, chlorophyll *a*. **k,l**, Representative chlorophyll fluorescence induction kinetics (**k**) and the corresponding ETR values (**l**) of the photothermal-released *M. aeruginosa* (photothermal, red line) and blank active *M. aeruginosa* (blank, blue line). The dark arrows indicate the application of a short pulse of saturating light and orange arrows indicate the activation (left) and deactivation (right) of actinic light. The lines in **l** represent the mean value. The scatter points and shaded areas around the lines represent the variation between the independent replicates (*n* = 6 for each group).

with a high harvesting efficiency exceeding 90%. For the case of excessive microalgae, the SMAG surface reaches adsorption saturation and is fully covered by single-layered microalgae (Fig. 3e). The maximum microalgal adsorption capacity (Q_m) of SMAG is determined to reach up to 1.5×10^6 cells mg_{SMAGs}^{-1}. Moreover, benefitting from efficient surface-specific modifications, the SMAGs with vastly different sizes showed similar microalgae adsorption capacity (Fig. 3f), allowing for customized size selection for various practical aquatic environments for efficient microalgae extraction.

Photothermal-driven desorption and regeneration
Unlike individual pieces, the magnetically collected SMAGs exhibit an accumulation-enhanced photothermal conversion (Fig. 4a) with

the temperature dramatically rising from 25 °C to 80 °C under 20 s irradiation (100 mW cm^{-2}). Thereafter, in contrast to the initial healthy microalgae (Fig. 4b,c), the intracellular structures of *M. aeruginosa* microalgae were severely damaged after 2 min photothermal treatment mediated by the SMAGs, including ruptured thylakoids, destructed cyanophycin granules and separation between the cell wall and membrane (Fig. 4d). However, the cell wall and membrane of *M. aeruginosa* microalgae remained intact after photothermal treatment (Fig. 4c,e), preventing the potential release of intracellular substances during the treatment. The impaired *M. aeruginosa* microalgae were found to be readily removed from the SMAGs surface through a simple water rinse (insert in Fig. 4a). Notably, the originally negative zeta potential of the *M. aeruginosa* microalgae significantly changed after the photothermal

treatment (Supplementary Fig. 14), which is believed to reduce the electrostatic attraction, thereby facilitating desorption.

To offer indirect insights into the origin of the unique photothermal-enabled desorption, we developed an in situ mechanical measurement of a single microalga using an atomic force microscope (AFM; Fig. 4f,g). Before photo irradiation, the microalga surface displays elastic mechanical characteristics, featuring a laconical pull-off behaviour with negligible energy dissipation during the tip retraction process (Fig. 4f). This reflects the outstanding toughness of the intact complex layer of extracellular polymeric substances (EPSs). The EPS layer, comprising various organic molecules such as carbohydrates, proteins, lipids and nucleic acids[35], imparts a negatively charged surface to the microalgae due to the accumulation of surface hydroxyl, carboxylic and amine functional groups[29]. Notably, the elasticity modulus of the EPS layer obviously decreases with prolonged photothermal treatment (Fig. 4f). Meanwhile, the tip withdrawal process becomes increasingly difficult, evidenced by the heightened energy dissipation and rupture distance (Supplementary Table 2) along with identified jumps and tethers in the withdraw curves (Fig. 4f). These characteristics are attributed to the mechanical extraction and unfolding processes of proteins in the outer EPS layer. All the evidence confirms the breakdown in the integrity of the microalgae EPS layer after the photothermal treatment, including direct EPS protein denaturation and mucilage layer destruction at high temperatures. The destruction of the EPS layer, which is responsible for the negatively charged surface of the microalgae, led to the significantly decreased negative surface charge density, resulting in the changed zeta potential[29].

The smooth microalgae surface concomitantly becomes much rougher with the generation of numerous small facets (Fig. 4h and Supplementary Fig. 15). Further angle distribution analysis of these facets reveals their anisotropy (Fig. 4i), which confirms the micro-cracks on the algae surface caused by the geometric discontinuity of the facets (Supplementary Fig. 15d). Taken together, the photothermal-enabled desorption originates from the functional protein denaturation in the EPS layer, thus directly destroying these charge-determined molecules inside or indirectly affecting the effective ionization of their functional groups. This leads to a significant decrease in negative-charge density or even a charge turnover on the microalgae surface (Supplementary Fig. 14). Furthermore, the *M. aeruginosa* microalgae spontaneously released from SMAGs retained their cell membrane and cell wall intact, preserving the valuable biomass for subsequent resource utilization.

The severe internal structural damages suggest the functional imperfections of the microalgae, prompting us to incidentally investigate their activities after photothermal treatment. By monitoring the real-time absorption spectrum of the microalgae adsorbed on SMAG during the photothermal treatment, it was observed that the phycobiliprotein (PBP) and carotenoid (Car) undergo rapid and significant degradation, which can result in detrimental effects to the microalgae's photosystems (Fig. 4j)[36,37]. This causes the visible colour to shift in the microalgae from green to yellow and dark brown (Supplementary Fig. 15). Judging from the chlorophyll fluorescence induction kinetics, different from the blank active microalgae, negligible changes in fluorescence can be detected for the photothermal-treated *M. aeruginosa* by turning on a saturation pulse light (Fig. 4k and Supplementary Table 3). Additionally, light-response curves for the electron transport rate (ETR), photosystem II (PSII) photochemical efficiency and non-photochemical quenching, along with the quantum yield of non-photochemical losses parameters (Fig. 4l and Supplementary Fig. 16) further corroborates the photothermal treatment-induced functional impairment of the overall photosynthetic system. This arises from the inactivation of PBPs and Cars, inhibiting the pathway for absorbing and utilizing light energy[38]. While it is an accompanying result of photothermal desorption, the deactivation process carries substantial practical value as it can pre-emptively prevent secondary contamination that may occur from potential microalgae spillage. Driven solely by

the simple photothermal effect, all these results confirm the effective regeneration of the SMAGs and concomitant microalgae deactivation, without detectable changes in adsorption behaviour and original properties (Supplementary Note 2 and Supplementary Figs. 17–20).

Scale-up implementation of outdoor microalgae extraction

Beyond the simulated laboratory condition, we quantified the practical performance of the SMAGs in a simulated outdoor environment (Fig. 5a). A glass aquarium holding 1,500 ml of water, containing 1.2×10^6 cells ml^{-1} of *M. aeruginosa* microalgae, was placed on a shade-free lawn, allowing for unobstructed sunlight exposure. Real-time solar irradiation intensity and water temperature were recorded using integrated sensors. To mimic a natural water body system, a mechanical propeller was used to introduce continuous and non-periodic disturbance, simulating random and irrotational low-frequency variations (Fig. 5b). The introduced SMAGs (1.25 g) could then navigate through the entirety of the aqueous space driven by these disturbances. These suspended SMAGs can be on-demand collected by an active electromagnet with an efficiency of 273 SMAGs l^{-1} T^{-1} s^{-1} (Supplementary Fig. 21). In comparison with the blank water body, it is worth mentioning that the addition of SMAGs with localized photothermal effect has negligible influence on the water temperature, thus eliminating concerns about potential physical stress on aquatic organisms and ecosystems caused by temperature changes (Fig. 5c).

Over 1.5 h implementation, three cycles of alternate microalgae adsorption and photothermal desorption using the recyclable SMAGs were conducted. The apparent clearance ratio of microalgae can reach 94% in the simulated bulk water body (Fig. 5c). Driven by the natural solar irradiation, the remarkable photothermal conversion of the magnetically collected SMAGs (insets in Fig. 5c) allows for the concentrated inactivation and on-demand desorption of microalgae. Besides the visual changes in the intracellular structures (Fig. 5d), the ultraviolet–visible (UV–Vis) absorption spectra confirm the photothermal deactivation of the desorbed microalgae during every cycle operation, featuring typical PBP destruction (Fig. 5e). Through simple rinsing, these widely dispersed microalgae were substantially concentrated, reducing spatial dispersity by about 107 times (inset in Fig. 5f and Supplementary Fig. 22). Undoubtedly, the SMAGs-mediated microalgae extraction significantly diminishes the turbidity and the microalgae and microcystin concentration of the target water, thus contributing to harmful algae control and water bloom remediation (Fig. 5f and Supplementary Fig. 23). Considering the variation of actual natural light intensity, we experimentally determined the cutoff solar irradiation intensity (SI) for the successful operation of this technique to be 35 mW cm^{-2} (Supplementary Fig. 24), which can induce the minimum temperature of 42 °C, leading to the desirable deactivation of most microalgae[39]. Since such SI is typically available in most climatic zones[40], this assures the wide applicability of the SMAGs in different geographical locations.

Considering the practical feasibility for covering a natural water body of a large volume, we further constructed the conceived extraction device by synergistically integrating the characteristics of the SMAGs (Figs. 1 and 5g and Supplementary Fig. 25). Powered solely by solar cells, the self-cruising device has proven highly effective in extracting microalgae in a 200 m^3 pond under a eutrophic state (chlorophyll *a*: 58 μg l^{-1}; Fig. 5g–i and Supplementary Figs. 26 and 27), which depends on continuous magnetic collection of the SMAGs underwater (Fig. 5i), solar-driven photothermal regeneration and microalgae concentrating (Supplementary Note 3). After magnetically removing the SMAGs, these desorbed microalgae with high enrichment formed large floc aggregates (Fig. 5h and Supplementary Figs. 28 and 29), which implies the decrease in their surface charge densities. Excluding some non-algae inorganic particulates, bacteria and protozoa (Supplementary Figs. 30 and 31), 89.6% of the extracted species are microalgae (Fig. 5j), generally including typical cyanobacteria, green algae, diatoms and
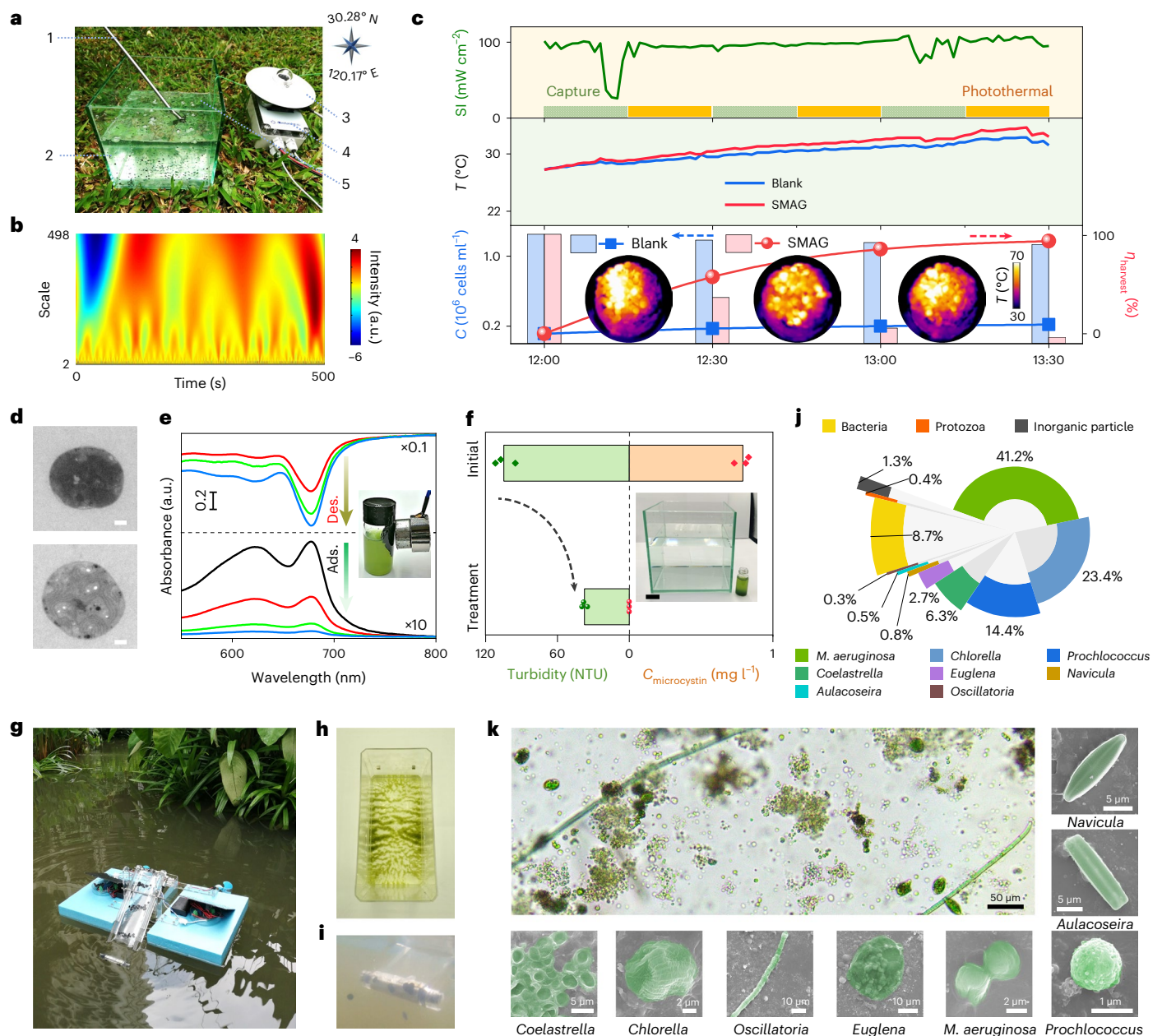
Fig. 5 | SMAGs-mediated microalgae extraction in outdoor operations.
a, A digital photo of the installation for simulating microalgae extraction in a natural environment. Key components include the mechanical stirrer (1), 1.25 g of the SMAGs dispersed in 1,500 ml of the *M. aeruginosa* microalgae-containing suspension (2), pyranometer (3), data logger (4) and K-type thermocouple (5). **b**, Continuous wavelet analysis of simulated water disturbances. **c**, Cycling microalgae adsorption and photothermal regeneration of the SMAGs under natural sunlight. The solar irradiation intensity (SI), the water body temperature (T) compared with that of the blank control along with the microalgae concentration (C, column) and the corresponding harvesting efficiency ($\eta_{harvest}$, line) are recorded. The insets show thermal images of the electromagnet-collected SMAGs irradiated under sunlight for 15 min. **d**, TEM images of the initial microalgae collected from the glass aquarium (bottom) and the harvested microalgae in the vial (top). Scale bars, 50 nm. **e**, UV–Vis absorption spectra of the microalgae suspensions in the glass aquarium and in the vial for three operating cycles. The inset shows the magnetic removal of the SMAGs from the vial after microalgae desorption. **f**, The comparison of turbidity and microcystin concentration between the initial bulk water and post-SMAGs-mediated microalgae extraction. The bars show the mean values of $n = 3$ for each group. The inset shows a digital photo of the treated bulk water in comparison to the vial containing the harvested microalgae. Scale bar, 2 cm. **g**–**i**, Photographs of the solar-powered self-cruising device for continuous microalgae extraction floating on a natural pond (**g**), the harvested microalgae after 2 h of operation (**h**) and a close-up of the magnetic collection of the SAMGs underwater (**i**). **j**, Statistics of the species harvested by the SMAGs from the natural pond. **k**, Overall optical microscopic image (top left) of the harvested microalgae suspension, complemented by pseudo-colored SEM images depicting representative microalgae.

euglenozoa (Fig. 5k). The exceptional selectivity is attributed to the scarcity of non-living particles/organisms, such as algae, possessing a high-density negative surface in natural surface water bodies (Supplementary Note 3 and Supplementary Table 1). Beyond the current electrostatic capture, the functional surface modification of SMAG, such as membrane protein-targeting molecules, can further increase the selectivity towards microalgae, potentially enabling specific microalgae extraction. It is worth mentioning that the recovery rate of the SMAGs remains up to 97.5% after a three-time cyclic utilization through the floating device (Supplementary Fig. 32). More importantly, the

regenerated SMAGs from the natural environment maintains the same level of stability in its suspended state as it had in its initial condition (Supplementary Fig. 32).

Conclusion

The proposed SMAGs-mediated on-site microalgae extraction provides a highly efficient, environmentally friendly, economical (Supplementary Note 4) and flexibly scalable strategy over post-bloom treatment techniques for proactive water bloom prevention (Supplementary Fig. 33 and Supplementary Note 5)[12]. The flexible design in the density, shape and size of the SMAGs allows for customized production to suit various water bodies of different scales. Suspension at the targeted water depth, where microalgae with a high-density negative surface charge predominate, distinguishing them from other non-living particles or organisms, gives SMAGs practical applicability to selective microalgae extraction, which can be further improved by specific surface modifications (Supplementary Notes 6 and 7). The synergistic integration of SMAGs with the self-cruising floating system could realize continuous microalgae extraction from natural water, contributing to the control and remediation of algae blooms in an unsupervised manner (Fig. 5g–k and Supplementary Note 7). Beyond providing a sustainable technique for conserving water resources and simultaneously extracting precious biomass for improved water management and capitalization, the concept of photothermal-driven desorption may inspire potential solutions for industrial adsorbents, paving the way for a greener and more energy-efficient adsorbent industry.

Methods

Materials and reagents

All the experimental chemicals were used as received without further purification. Ferric chloride (98%), polyvinylpyrrolidone (average molecular weight of 55,000), pluronic F-127, sodium borohydride (99%) and (3-aminopropyl)triethoxysilane (99%) were purchased from Sigma-Aldrich.

Synthesis of FeNPs

The amorphous FeNPs were synthesized via a modified Hubble-bubble reduction process[30]. First, 2 g of polyvinylpyrrolidone and 0.8 g of F-127 were added into 60 ml of FeCl₃ aqueous solution (0.05 M) under stirring. After the solution became clear, it was placed in an ice bath and bubbled with Ar to remove the dissolved oxygen. Then, 10 ml of sodium borohydride (1 M) aqueous solution was drop-wise added into the mixture by a peristaltic pump with a drip feed speed of 5 µl s⁻¹. The rapid generation of H₂ created numerous bubbles, and the subsequent reduction reaction resulted in the formation of FeNPs on the surface of the bubbles. Next, 10 ml of ethanol was added as a demulsifier to disrupt the black bubbles. The resultant FeNPs were collected by magnetic separation, washed three times with ethanol and subsequently dispersed in deoxygenated ethanol.

Fabrication of SMAGs

The procedure for fabricating the SMAGs begins with the preparation of a membrane containing FeNPs and PDMS on aqueous surface[41]. First, 0.08 g of FeNPs was mixed with 1.5 g of silicone elastomer base and 0.15 g of curing agent (Sylgard, Dow Corning) under stirring in a vacuum chamber. Then, 100 µl of the mixed solution was dripped onto the water surface in a glass container. The solution spreads quickly and evenly over the water's surface. After curing at 60 °C for 3 h, a robust membrane was formed on the water surface (Fe–PDMS). The PDMS membrane was synthesized under the same conditions without the addition of FeNPs.

The synthesized Fe–PDMS membranes were cleaned in deionized (DI) water and dried under a nitrogen stream. Subsequently, they were placed in a plasma reactor connected to an O₂ gas cylinder and treated for 2 min. Hydroxyl (–OH) functional groups were introduced onto the

surface of the Fe–PDMS through O₂ plasma treatment (OH–Fe–PDMS). The OH–Fe–PDMS membranes were immersed into (3-aminopropyl) triethoxysilane solution (1 vol% in ethanol) and reacted at 40 °C for 40 min to synthesize amine functionalized Fe–PDMS (SMAG). After that, the obtained SMAG membranes were rinsed with ethanol and DI water several times and dried at room temperature.

The uniformly sized SMAGs were produced by a laser cutter machine. The SMAG membrane was placed onto a laser cutter machine (Diaotu). A circular pattern was loaded into the laser cutter software, and the laser power was set to 10 W. The laser then cuts through the membrane, creating SMAGs with precise uniform dimensions.

Density calculation

The density of SMAGs (ρ, g cm⁻³) could be customized by adjusting the integrated FeNPs content and porosity, which could be calculated according to the following equation:

$$\rho = \frac{1-b}{\frac{a}{\rho_{Fe}} + \frac{1-a}{\rho_{PDMS}}} \tag{1}$$

where a and b are the Fe content and porosity of SMAGs, respectively; ρ_{Fe} denotes the density of Fe, which is 7.874 g cm⁻³; and ρ_{PDMS} denotes the density of PDMS, which is 0.965 g cm⁻³. The related data extraction and further processing were realized using a customized MATLAB code.

Material characterizations

SEM images and energy-dispersive X-ray spectroscopy were obtained on a field-emission scanning electron microscope (Zeiss Sigma 300). The samples were fixed on a silicon wafer and coated with Pt for SEM measurements. TEM images, high-resolution TEM images and selected-area electron diffraction patterns were acquired by a JEM-200 CX transmission electron microscope at 200 kV. The topography image and corresponding geometrical angle distributions were performed on a Bruker JPK NanoWizard Sense AFM. X-ray diffraction patterns were obtained using Cu Kα radiation (λ = 0.154178 nm) at 40 kV and 40 mA, with a scanning rate of 4° min⁻¹ (Rigaku SmartLab). Diffuse reflectance spectra were measured on a Shimadzu UV3600 spectrometer, using BaSO₄ as a reference. Fourier-transform infrared spectra were obtained on a Thermofisher Nicolet iS20 Fourier-transform infrared spectrometer. Zeta potentials of the materials were measured by a surface zeta potential analyser (Anton Paar SurPASS 3). Contact angle measurements were carried out on a contact angle determinator (Lunderskov). Automatically titration of 8 µl of droplets deposited on the surface of the material, images were acquired every 50 ms. The 3D tomographic reconstitution images of SMAGs were taken by an optical microscope with focus stacking (CX43, Olympus). The corresponding Feret properties of the network and geometric heat diffusion simulation were performed on a customized MATLAB application. The static compressive behaviour and cyclic compress force (F) measurements were carried on a versatile tensile tester (MultiTest-i, Mecmesin) at a constant speed of 10 cm min⁻¹. The compression area (A) was 0.03 mm². The compress stress (s) was calculated from the relation of $s = F/A$.

Microalgae culture and analysis

The algae and culture medium were obtained from the Freshwater Algae Culture Collection at the Institute of Hydrobiology (FACHB), National Aquatic Biological Resource Center (Wuhan, China), including the axenic strains of *M. aeruginosa* (FACHB-526) and the corresponding sterile culture medium BG11. *M. aeruginosa* microalgae were cultured in the sterile BG11 medium in a light incubator with a 12:12 h light-dark regime. Illumination (3,000 lux) was provided by cool-white light-emitting diode lights. The temperature was maintained at 25 ± 1 °C. The cells were collected by filtration (0.22 m Stericup; Millipore) during their mid-logarithmic growth phase and suspended in a fresh growth medium for experiments.

The concentration of microalgae (C_{algae}) could be calculated by measuring the optical density at 680 nm (OD_{680}) based on the linear correlation between OD_{680} and C_{algae}. The relationship between OD_{680} and C_{algae} could be determined by diluting microalgae suspension with BG11 or concentrating via centrifugation to get different concentrations. The C_{algae} was determined by counting cell numbers in a haemocytometer chamber. OD_{680} was measured on a UV–Vis spectrometer (Shimadzu UV3600). Three independent biological replicates were performed for each concentration.

Microalgae harvesting performance evaluation

A specific quantity of either SMAGs or Fe–PDMS with the same sizes (diameter of 1 mm and thickness of 73 µm), varying from 0 g to 1.2 g, was dispersed in an 80 ml *M. aeruginosa* microalgae suspension in a glass flask. The flask was then placed on a rotary shaker and agitated at 200 rpm for 15 min at a temperature of 25 ± 1 °C. Then, the materials were magnet collected and separated from the suspension using a permanent magnet (NdFeB, 10 × 5 cm) for 2 min. The concentration of initial microalgae suspension and after the treatment was assessed by measuring the OD_{680} values, which allowed for the determination of the corresponding C_{algae} based on their established relationship. The harvesting efficiency ($\eta_{harvest}$) could be calculated according to the following equations.

$$\eta_{harvest} = (1 - C_e/C_0) \qquad (2)$$

where C_0 was the initial microalgae concentration (cells ml^{-1}), and C_e was the microalgae concentration after the harvesting process (cells ml^{-1}).

Adsorption isotherm experiments were carried out in a range of *M. aeruginosa* concentrations by dilution with BG11 or concentration via centrifugation. SMAGs (0.72 g) were dispersed into 80 ml *M. aeruginosa* microalgae suspension. The concentration of microalgae cells (10^6 cells ml^{-1}) ranged from 2.1 to 15.5. The adsorption capacity (Q_e, cells mg$_{SMAGs}$$^{-1}$) could be calculated according to the following equations:

$$Q_e = (C_0 - C_e)/C_{SMAG} \qquad (3)$$

where C_0 was the initial microalgae concentration (cells ml^{-1}), C_e was the equilibrium microalgae concentration (cells ml^{-1}) and C_{SMAG} was the dosage of SMAGs (mg ml^{-1}) used for the microalgae harvesting. The Langmuir isotherm model was used for fitting experimental data. It could be expressed in a nonlinear form according to the following equations:

$$Q_e = Q_m K_L C_e/(1 + K_L C_e) \qquad (4)$$

where Q_m (cells per mg$_{SMAGs}$) was the maximum adsorption capacity and K_L was the Langmuir constant. Three independent biological replicates were performed for each concentration.

To assess the size influence on the adsorption capacities of the SMAGs, SMAGs with different diameters while the same thickness (73 µm) were prepared by a laser cutter, with diameters ranging from 0.1 cm to 3 cm. Then, 0.72 g of the SMAGs, all of the same size, were dispersed into 80 ml *M. aeruginosa* microalgae suspension with a cell concentration of 1.35×10^7 cells ml^{-1}. After being agitated at 200 rpm for 15 min at 25 ± 1 °C, the SMAGs were magnet collected and separated from the suspension using a permanent magnet. The adsorption capacity (Q_e, cells mg$_{SMAGs}$$^{-1}$) of the SMAGs with different sizes could be calculated according to equation (3). Five independent biological replicates were performed for each concentration.

Microalgae–SMAG interaction characterization

To investigate the interaction between *M. aeruginosa* microalgae and SMAG, a microalga adsorbed on the SMAG was characterized using a reconstruction technique based on the secondary electron scattering intensity of SEM. The samples were immersed in a 2.5% glutaraldehyde in a 0.1 M phosphate buffer at 4 °C overnight, followed by rinsing them with a 0.1 M phosphate buffer. Next, the samples were post-fixed with 1% osmium in a 0.1 M phosphate buffer at 4 °C for 4 h and rinsed with 0.1 M phosphate buffer. Subsequently, the samples were dehydrated for 15 min in each of the graded concentrations of ethanol (50%, 70%, 80%, 90% and 95%), followed by 20 min dehydrated with anhydrous ethanol. After supercritical drying, the morphologies of the microalgae were observed using a field-emission SEM (Zeiss Sigma 300). The pseudo-colour image was based on secondary electron scattering intensity. The scattering intensity was calibrated by a Pt-coated silicon wafer. The image reconstruction and line profile extraction were realized by a customized MATLAB code. A microalga adsorbed on the Fe–PDMS was characterized by the same process as the control.

Photothermal regeneration and mechanism analysis

The photothermal performance of microalgae-adsorbed SMAGs was evaluated by irradiating them under a 300 W Xe light source with an Air Mass 1.5 G filter (AM 1.5 G, 100 mW cm^{-2}). The temperature changes and thermal images were recorded by a thermal imaging camera (FLIR E96). The regeneration of microalgae-adsorbed SMAGs was conducted by exposing them to 2 min irradiation (AM 1.5 G, 100 mW cm^{-2}), followed by rinsing with DI water. The morphology of the treated microalgae was characterized using SEM and TEM. For SEM observations, the samples were pre-treated using the method mentioned in the section 'Microalgae–SMAG interaction characterization'. For TEM observations, samples were fixed with 3% glutaraldehyde in 0.1 M cacodylate buffer at 4 °C for 4 h, then post-fixated in 1% osmium–tetroxide in a 0.1 M phosphate buffer at 4 °C for 2 h. After rinsing with a 0.1 M phosphate buffer, the samples were dehydrated in a graded ethanol series with ethanol concentrations of 30%, 50%, 70%, 80%, 90% and 100% before being embedded in Epon resin. Then, ultrathin sections of approximately 70 nm were prepared and examined by TEM (JEOL Ltd.). The zeta potential of the microalgae was measured on a Zetasizer (Zetasizer Nano S90, Malvern).

To gain a fundamental understanding of the photothermal regeneration, the change of adsorbed *M. aeruginosa* microalgae on the SMAG was monitored by the AFM and a UV–Vis spectrometer during the light irradiation (AM 1.5 G, 100 mW cm^{-2}). The topography image and the mechanical measurement of microalgae were performed on a Bruker JPK NanoWizard Sense AFM using an AC240-PP tip (OPUS, nominal spring force constant of 2 N m^{-1}). The actual spring constant was calibrated by acquiring a force–distance curve on a clean hard glass surface. The loading and unloading rates were 1 µm s^{-1} with a sample rate of 2,048 Hz. The UV–Vis absorption spectra of adsorbed *M. aeruginosa* microalgae on the SMAG during irradiation (AM 1.5 G, 100 mW cm^{-2}) were obtained on a spectrometer (HR4, Ocean Insight) with a Xenon light source (HPX-2000, Ocean Insight).

The activity of desorbed *M. aeruginosa* microalgae was analysed by measuring their chlorophyll fluorescence using an imaging pulse amplitude modulated fluorometer (I-PAM, Walz). A 200 µl aliquot of the collected desorbed microalgae suspension was withdrawn and transferred to a 96-well plate. Measurements were carried out under well-defined laboratory conditions within 15 min of short dark adaptation. At first, minimal and maximal fluorescence (F_o and F_m) were determined by a saturation pulse. After that, actinic light (400 µmol photons m^{-2} s^{-1}) was switched on to determine the steady-state fluorescence (F). Saturation pulses with a width of 600 ms were applied to determine maximal fluorescence (F_m'). Then, the actinic light was switched off to determine minimal fluorescence (F_o'). The PSII photochemical efficiency (a.u.), non-photochemical quenching (a.u.) and quantum yield of other non-photochemical losses were recorded. The ETR through PSII (a.u) was recorded under 0 to 804 µmol photons m^{-2} s^{-1}. For comparison, the chlorophyll fluorescence of *M. aeruginosa* microalgae under 2 min

irradiation (AM 1.5 G, 100 mW cm^{-2}) was measured. The measurements were taken independently from six biological replicates to ensure the accuracy of the results.

Outdoor tests in a simulated water body
A glass aquarium (14 ×14 × 10 cm) filled with 1,500 ml of *M. aeruginosa* microalgae suspension at a concentration of $1.2 × 10^6$ cells ml^{-1} was placed on a lawn, free from obstruction by trees or buildings, ensuring unblocked sunlight exposure (at the geographical coordinates of 120.17°E longitude and 30.28°N latitude). Then, 1.25 g of SMAGs with a diameter of 5 mm were added into the microalgae suspension, while a mechanical propeller provided continuous, non-periodic agitation to mimic water flow. Real-time solar irradiation intensity and water temperature were monitored using a flat pyranometer (LPPYRA-Lite, Delta OHM) and a K-type thermocouple respectively, with data recorded every 30 s by a wireless data logger (HD35, Delta OHM). After 15 min, the dispersed SMAGs were collected by an active electromagnet and exposed to natural sunlight for another 15 min. The temperature and thermal images of the electromagnet-collected SMAGs were captured by a thermal imaging camera (FLIR E96). Subsequently, SMAGs were immersed in 15 ml of DI water in a vial for microalgae desorption. The regenerated SMAGs were readded into the 1,500 ml microalgae suspension for two additional cycles, and the procedures were repeated. The UV–Vis absorption spectra of microalgae suspension in the glass aquarium or desorbed in the vial were recorded on a Shimadzu UV3600 spectrometer for each cycle. For accurate UV–Vis absorption measurements, the *M. aeruginosa* microalgae suspension in the glass aquarium was concentrated tenfold using centrifugation, while the desorbed microalgae suspension in the vial was diluted tenfold by DI water. The microalgae suspension concentration and harvesting efficiency ($\eta_{harvest}$) were determined using the method outlined in the section 'Microalgae harvesting performance evaluation'. The blank control was carried out under the same conditions without the addition of SMAGs.

The turbidity was measured by a turbidity meter (Oakton T-100). Liquid (10 ml) was withdrawn from the glass aquarium after stirring, and filtered through a 0.45 μm cellulose acetate membrane for the measurement. The concentration of microcystin was analysed by high-performance liquid chromatography (e2695, Waters). Liquid (5 ml) was withdrawn from the glass aquarium after stirring. The liquid was subjected to three freeze/thaw (−20 °C/25 °C) cycles to achieve complete cell lysis. The samples were then centrifuged at 6,800*g* for 10 min at 25 °C. The supernatant was filtered through a 0.45 μm cellulose acetate membrane. Chromatographic separation of microcystins was carried out using a Zorbax Water X bridge TM C18 column (5 μm, 4.6 × 250 mm) maintained at 30 °C, at a flow rate of 1 ml min^{-1}, with a gradient of pure methyl alcohol (solvent A) and 0.05% trifluoroacetic acid in water (solvent B). The solvent program was as follows: 65% A and 35% B for the entire 15 min period. The injected sample volume was 10 μl, and the detection was performed with a diode array UV detector at 238 nm. The concentrations of microcystin were quantified by the calibration curve derived from the 'Microcystins-LR standard' (MC-LR, Macklin).

Implementation in natural water body
A natural pond (dimension of ~10 × 10 m and ~2 m in water depth) under a eutrophic state (chlorophyll *a*: 58 μg l^{-1}) was employed to test the floating device for continuous microalgae extraction. Briefly, 11.669 g of the discal SMAGs with 6 mm in diameter and 73 μm in thickness were firstly scattered in the pond. After 15 min, the floating device (Supplementary Figs. 24 and 25 and Supplementary Note 3) started to collect the suspended SMAGs in a self-cruising manner. The cruising speed was set at about 2 m min^{-1}. According to the suspended depth of the SMAGs, the immersed depth of the liner bearing was set at 10 cm with the inclination angle of polyethylene conveyer of 45°. The rotation interval of the magnet-equipped liner bearing was 2.5 min with a rectilinear speed of the polyethylene conveyer of 60 cm min^{-1}.

The vessel was initially filled with DI water at 180 ml in volume. During the 2 h operation, the time-course climate parameters including local air temperature, air velocity, humidity and barometric pressure were recorded by a TSI 9565-P VelociCalc multi-function ventilation meter. The solar irradiance was recorded using a flat pyranometer (LPPYRA-Lite, Delta OHM).

During the collecting period, a piece of the microalgae-adsorbed SMAG collected from the liner bearing was used for optical microscopy and SEM observation. The collected SMAGs were magnetically separated by using a magnet and scattered into the pond again every 40 min. At the end, the SMAGs were magnetically separated, washed with DI water and then let dry at 50 °C for 1 h. The microalgae suspension in the vessel was characterized by UV–Vis spectrophotometry, optical microscopy and SEM. Statistics of non-algae species and different kinds of recognizable microalgae were based on the shape and dimension in SEM images with the assistance of energy-dispersive X-ray spectroscopy element analysis.

Data availability
The data supporting the findings of this study are available within the paper (and its Supplementary Information).

References
1. Maso, M. & Garcés, E. Harmful microalgae blooms (HAB); problematic and conditions that induce them. *Mar. Pollut. Bull.* **53**, 620–630 (2006).
2. Sellner, K. G., Doucette, G. J. & Kirkpatrick, G. J. Harmful algal blooms: causes, impacts and detection. *J. Ind. Microbiol. Biotechnol.* **30**, 383–406 (2003).
3. Hou, X. et al. Global mapping reveals increase in lacustrine algal blooms over the past decade. *Nat. Geosci.* **15**, 130–134 (2022).
4. Berdalet, E. et al. Marine harmful algal blooms, human health and wellbeing: challenges and opportunities in the 21st century. *J. Mar. Biol. Assoc. UK* **96**, 61–91 (2016).
5. Chapra, S. C. et al. Climate change impacts on harmful algal blooms in US freshwaters: a screening-level assessment. *Environ. Sci. Technol.* **51**, 8933–8943 (2017).
6. Riebesell, U. et al. Toxic algal bloom induced by ocean acidification disrupts the pelagic food web. *Nat. Clim. Change* **8**, 1082–1086 (2018).
7. Dai, Y. et al. Coastal phytoplankton blooms expand and intensify in the 21st century. *Nature* **615**, 280–284 (2023).
8. Treuer, G., Kirchhoff, C., Lemos, M. C. & McGrath, F. Challenges of managing harmful algal blooms in US drinking water systems. *Nat. Sustain.* **4**, 958–964 (2021).
9. Glibert, P. M. & Burford, M. A. Globally changing nutrient loads and harmful algal blooms: recent advances, new paradigms, and continuing challenges. *Oceanography* **30**, 58–69 (2017).
10. Anantapantula, S. S. & Wilson, A. E. Most treatments to control freshwater algal blooms are not effective: meta-analysis of field experiments. *Water Res.* **243**, 120342 (2023).
11. Williams, P. Jl. B. & Laurens, L. M. Microalgae as biodiesel & biomass feedstocks: review & analysis of the biochemistry, energetics & economics. *Energy Environ. Sci.* **3**, 554–590 (2010).
12. Qu, M. et al. Algal blooms: proactive strategy. *Science* **346**, 175–176 (2014).
13. Darvehei, P., Bahri, P. A. & Moheimani, N. R. Model development for the growth of microalgae: a review. *Renew. Sust. Energy Rev.* **97**, 233–258 (2018).
14. Bhola, V., Swalaha, F., Ranjith Kumar, R., Singh, M. & Bux, F. Overview of the potential of microalgae for CO$_2$ sequestration. *Int. J. Environ. Sci. Technol.* **11**, 2103–2118 (2014).
15. Zhao, B. & Su, Y. Process effect of microalgal–carbon dioxide fixation and biomass production: a review. *Renew. Sust. Energy Rev.* **31**, 121–132 (2014).

16. Zhu, L. Biorefinery as a promising approach to promote microalgae industry: an innovative framework. *Renew. Sust. Energy Rev.* **41**, 1376–1384 (2015).

17. Barros, A. I., Gonçalves, A. L., Simões, M. & Pires, J. C. Harvesting techniques applied to microalgae: a review. *Renew. Sust. Energy Rev.* **41**, 1489–1500 (2015).

18. Singh, G. & Patidar, S. Microalgae harvesting techniques: a review. *J. Environ. Manage.* **217**, 499–508 (2018).

19. Abu-Shamleh, A. & Najjar, Y. S. Optimization of mechanical harvesting of microalgae by centrifugation for biofuels production. *Biomass Bioenergy* **143**, 105877 (2020).

20. Zhao, F. et al. Microalgae harvesting by an axial vibration membrane: the mechanism of mitigating membrane fouling. *J. Membrane Sci.* **508**, 127–135 (2016).

21. Zhao, Z., Muylaert, K. & Vankelecom, I. F. Combining patterned membrane filtration and flocculation for economical microalgae harvesting. *Water Res.* **198**, 117181 (2021).

22. Laamanen, C. A., Ross, G. M. & Scott, J. A. Flotation harvesting of microalgae. *Renew. Sust. Energy Rev.* **58**, 75–86 (2016).

23. Alkarawi, M. A., Caldwell, G. S. & Lee, J. G. Continuous harvesting of microalgae biomass using foam flotation. *Algal Res.* **36**, 125–138 (2018).

24. Vandamme, D., Foubert, I. & Muylaert, K. Flocculation as a low-cost method for harvesting microalgae for bulk biomass production. *Trends Biotechnol.* **31**, 233–239 (2013).

25. Matter, I. A. et al. Flocculation harvesting techniques for microalgae: a review. *Appl. Sci.* **9**, 3069 (2019).

26. Balaji-Prasath, B. et al. Methods to control harmful algal blooms: a review. *Environ. Chem. Lett.* **20**, 3133–3152 (2022).

27. Suparmaniam, U. et al. Insights into the microalgae cultivation technology and harvesting process for biofuel production: a review. *Renew. Sust. Energy Rev.* **115**, 109361 (2019).

28. Van Dolah, F. M. Marine algal toxins: origins, health effects, and their increased occurrence. *Environ. Health Perspect.* **108**, 133–141 (2000).

29. Li, N. et al. Electrostatic charges on microalgae surface: mechanism and applications. *J. Environ. Chem. Eng.* **10**, 107516 (2022).

30. Zhang, C. et al. Synthesis of iron nanometallic glasses and their application in cancer therapy by a localized Fenton reaction. *Angew. Chem. Int. Ed.* **55**, 2101–2106 (2016).

31. Wang, X. Q. et al. Nanophotonic-engineered photothermal harnessing for waste heat management and pyroelectric generation. *ACS Nano* **11**, 10568–10574 (2017).

32. Grinstaff, M. W., Salamon, M. B. & Suslick, K. S. Magnetic properties of amorphous iron. *Phys. Rev. B* **48**, 269 (1993).

33. Zhang, C. et al. Cryogenic exfoliation of non-layered magnesium into two-dimensional crystals. *Angew. Chem. Int. Ed.* **58**, 8814–8818 (2019).

34. Harke, M. J. et al. A review of the global ecology, genomics, and biogeography of the toxic cyanobacterium, microcystis spp. *Harmful Algae* **54**, 4–20 (2016).

35. Xiao, R. & Zheng, Y. Overview of microalgal extracellular polymeric substances (EPS) and their applications. *Biotechnol. Adv.* **34**, 1225–1244 (2016).

36. Domínguez-Martín, M. A. et al. Structures of a phycobilisome in light-harvesting and photoprotected states. *Nature* **609**, 835–845 (2022).

37. Zakar, T., Laczko-Dobos, H., Toth, T. N. & Gombos, Z. Carotenoids assist in cyanobacterial photosystem II assembly and function. *Front. Plant Sci.* **7**, 295 (2016).

38. Maxwell, K. & Johnson, G. N. Chlorophyll fluorescence-a practical guide. *J. Exp. Bot.* **51**, 659–668 (2000).

39. Béchet, Q., Laviale, M., Arsapin, N., Bonnefond, H. & Bernard, O. Modeling the impact of high temperatures on microalgal viability and photosynthetic activity. *Biotechnol. Biofuels* **10**, 1–11 (2017).

40. Coskun, C., Oktay, Z. & Dincer, I. Estimation of monthly solar radiation distribution for solar energy system analysis. *Energy* **36**, 1319–1323 (2011).

41. Zhang, C., Lu, W., Xu, Y., Zeng, K. & Ho, G. W. Mechanistic formulation of inorganic membranes at the air–liquid interface. *Nature* **616**, 293–299 (2023).